

Sensitivity of the FCC-ee to axion-like particles at different center-of-mass energies

Juliette Alimena^a Elnura Bakhishova^{a,b,c} Freya Blekman^{a,b} Jannah Darwish
Abdelhafiz^{a,g} Christina Dorofeev^{a,d} Jeremi Niedziela^{a,e} Giacomo Polesello^f
Anna Przybyl^{a,b} Lovisa Rygaard^{a,b}

^a*Deutsches Elektronen-Synchrotron DESY, Notkestr. 85, 22607 Hamburg, Germany*

^b*Institut für Experimentalphysik, Universität Hamburg, Luruper Chaussee 149, 22761 Hamburg, Germany*

^c*Department of Physics and Astronomy, University of Amsterdam, 1098 XH Amsterdam, The Netherlands*

^d*Institute of Fundamental Science, University of Oregon, 1585 E 13th Ave, Eugene, Oregon 97403, USA*

^e*Interuniversity Institute for High Energies (IIHE), Vrije Universiteit Brussel, Pleinlaan 2, 1050 Brussels, Belgium*

^f*INFN Sezione di Pavia, Via Agostino Bassi, 6, 27100 Pavia PV, Italy*

^g*Department of Mathematics, Faculty of Science, Cairo University, Giza 12613, Egypt*

E-mail: anna.przybyl@desy.de

ABSTRACT: The sensitivity of the proposed FCC-ee collider to axion-like particles (ALPs) is investigated at all planned center-of-mass energies, with focus on the case where the ALP couples primarily to electroweak gauge bosons at leading order. We study the associated production of the ALP with a photon, with the ALP decaying in turn to two photons, yielding a three-photon final state. The ALP coupling to the photon is evaluated for ALP masses of 5 to 320 GeV. In this effective model, the FCC-ee will be able to detect ALPs for couplings down to a few 10^{-6} GeV⁻¹ (10^{-5} GeV⁻¹) during the Z pole run (WW, ZH, and $t\bar{t}$ threshold runs). Additionally, this final state has the potential to probe the underlying electroweak structure of ALP couplings for ALP masses below the Z boson mass.

ARXIV EPRINT: [1234.56789](https://arxiv.org/abs/1234.56789)

Contents

1	Introduction	1
2	Theoretical framework	2
2.1	Axion-like particles	2
2.2	ALP model benchmark	3
3	Simulation	4
3.1	Event simulation	4
4	Event selection	5
4.1	Preselection	6
4.2	Final selection	7
5	Results	8
5.1	Primary results	8
5.2	Dependence of results on Wilson coefficients in Lagrangian	12
6	Summary and outlook	16
A	Appendix	17

1 Introduction

Although widely successful, the Standard Model (SM) of particle physics fails to explain certain experimental observations, such as the baryon asymmetry of the universe, dark matter, and non-zero neutrino masses. Additionally, certain theoretical aspects of the SM are not yet explained, such as the hierarchy problem, the strong CP problem, and flavor structure. These open questions can be addressed by direct observations of new physics (NP) or by measuring deviations from SM predictions, and call for an intensified collider exploration. A high-luminosity, energy frontier lepton collider would allow for precision studies of the electroweak sector, particularly the Higgs boson. The preferred option for the next generation of high-energy particle colliders is the Future Circular Collider (FCC) at CERN [1]. The electron-positron stage of the FCC, FCC-ee, would offer numerous opportunities for precision measurements and new-physics studies [2].

The FCC-ee is proposed to run at or around four different center-of-mass energies (E_{CM}): the Z pole (91 GeV), the WW threshold (160 GeV), the ZH production peak (240 GeV), as well as the $t\bar{t}$ threshold (340-365 GeV) [3, 4]. The collision environment will be clean and well-defined, which will allow for precision measurements that are sensitive to tiny deviations from the SM. The high integrated luminosity makes the FCC-ee an ideal

facility for the direct detection of NP, particularly for processes with small production cross sections or weak couplings that would otherwise be inaccessible. An exciting NP case that could be probed at the FCC-ee is that of long-lived particles, which could be produced in collisions and decay to particles with some measurable displacement from the primary interaction point. In Ref. [5], heavy neutral leptons, axion-like particles (ALPs), and exotic Higgs decays, all of which can produce long-lived particles in certain areas of the parameter space, are probed in the context of the FCC-ee.

The QCD axion, a pseudo-Nambu-Goldstone boson, was introduced in the 1970s to address the strong CP problem [6–9]. More generally, a broader class of pseudoscalar states, known as ALPs (a), occur in theories with spontaneously broken global symmetries, with ALP masses (m_a) and couplings to SM particles spanning many orders of magnitude [10, 11]. ALPs are particularly interesting because they provide a generic, but well-motivated, probe of NP across a wide range of energy scales. In certain regions of parameter space, ALPs can be dark matter candidates [12], and in others, they can be dark matter mediators [13, 14]. At the FCC-ee, the high luminosity at the Z pole run will allow us to probe small ALP couplings, while the higher center-of-mass energies (E_{CM}) will, in turn, allow us to probe larger m_a .

In the MeV-TeV mass range, ALPs are constrained by collider searches [15–24], beam-dump and fixed-target experiments [25–30], and astrophysical bounds from supernovae [31]. Collider searches can be split into two categories: searches via light-by-light scattering, performed at the ATLAS and CMS experiments, [18, 20], and searches where ALPs decay to photonic final states, performed at the FASER, BESIII, ATLAS, CMS, and LHCb experiments [15–17, 19, 21–24]. A combination of all current exclusions, as well as sensitivity projections for the ALP coupling to photons for BelleII, SHiP, ALICE, MuC, CLIC, LCF, and the FCC, can be found in Ref. [32]. In particular, sensitivity projections have been set for the FCC-ee in Refs. [33, 34]. An overview of ALP signatures at the LHC can be found in Ref. [35], while ALP signatures at future colliders CLIC, CEPC, FCC, SPPC, and MATHUSLA, are discussed in Ref. [11].

In this study, we focus on ALPs produced at the FCC-ee in association with a photon, $e^+e^- \rightarrow a\gamma$, and decaying to two photons, $a \rightarrow \gamma\gamma$. This final state has already been studied at the Z pole in a more involved analysis [33], and sensitivity projections have been set for m_a ranging from 0.1 to 85 GeV. The purpose of this study is to update the analysis at the Z pole and extend it to the proposed higher center-of-mass energy runs, such that the ALP mass probed is extended to 320 GeV.

2 Theoretical framework

2.1 Axion-like particles

The ALP is a pseudoscalar that appears in many SM extensions. The effective Lagrangian of the a coupling to a photon or Z boson after electroweak symmetry breaking can be defined as [11]

$$\mathcal{L}_{\text{eff}} \ni C_{\gamma\gamma} \frac{a}{\Lambda} F_{\mu\nu} \tilde{F}^{\mu\nu} + \frac{2e^2}{s_w c_w} C_{\gamma Z} \frac{a}{\Lambda} F_{\mu\nu} \tilde{Z}^{\mu\nu} + \frac{e^2}{s_w^2 c_w^2} C_{ZZ} \frac{a}{Z} Z_{\mu\nu} \tilde{Z}^{\mu\nu}, \quad (2.1)$$

where $c_w = \cos \theta_w$ and $s_w = \sin \theta_w$. Λ is the scale of new physics, $F_{\mu\nu}$ describes the photon in the broken phase of electroweak symmetry, and $Z_{\mu\nu}$ describes the Z boson in the broken phase of electroweak symmetry. The Wilson coefficients $C_{\gamma\gamma}$, $C_{\gamma Z}$, and C_{ZZ} satisfy

$$C_{\gamma\gamma} = C_{WW} + C_{BB}, \quad C_{\gamma Z} = c_w^2 C_{WW} - s_w^2 C_{BB}, \quad C_{ZZ} = c_w^4 C_{WW} + s_w^4 C_{BB}, \quad (2.2)$$

where C_{WW} is the Wilson coefficient for the ALP coupling to the unbroken $SU(2)$ gauge field, and C_{BB} is the Wilson coefficient for the ALP coupling to the unbroken $SU(1)$ gauge field.

2.2 ALP model benchmark

We adopt a model benchmark [11, 14] where the ALP couples primarily to electroweak gauge bosons by setting $C_{WW} = 0$. The Wilson coefficients now satisfy

$$C_{\gamma\gamma} = C_{BB}, \quad C_{\gamma Z} = -s_w^2 C_{BB}, \quad C_{ZZ} = s_w^4 C_{BB}, \quad (2.3)$$

and imply that the ALP couples almost exclusively to photons. We focus on the scenario where an ALP is produced in association with a photon, and the ALP itself decays into two photons. The differential production cross section for an ALP produced in association with a photon is given by [11]

$$\frac{d\sigma(e^+e^- \rightarrow a\gamma)}{d\Omega} = 2\pi\alpha\alpha^2(s) \frac{s^2}{\Lambda^2} \left(1 - \frac{m_a^2}{s}\right)^3 (1 + \cos^2\theta) (|V_\lambda(s)|^2 + |A_\lambda(s)|^2), \quad (2.4)$$

where m_a is the ALP mass, θ is the scattering angle of the photon relative to the beam axis, and \sqrt{s} is the center-of-mass energy. The vector and axial-vector form factors are given by

$$V_\lambda(s) = \frac{C_{\gamma\gamma}}{s} + \frac{g_V}{2c_w^2 s_w^2} \frac{C_{\gamma Z}}{s - m_Z^2 + im_Z \Gamma_Z}, \quad (2.5)$$

$$A_\lambda(s) = \frac{g_A}{2c_w^2 s_w^2} \frac{C_{\gamma Z}}{s - m_Z^2 + im_Z \Gamma_Z}, \quad (2.6)$$

where $g_V = 2s_w^2 - 1/2$, $g_A = -1/2$ and Γ_Z is the total width of the Z boson. The $\left(1 - \frac{m_a^2}{s}\right)^3$ factor leads to a rapid decrease in production as m_a approaches \sqrt{s} . The cross section at $s = m_Z^2$ is enhanced by a factor of $(m_Z^2/\Gamma_Z^2) \approx 1336$ compared to the cross section at $s \gg m_Z^2$ [5], and both of these features are shown in Figure 1 for $C_{BB} = 1$ and $C_{WW} = 0$.

At $m_a < m_Z$, the only decay mode possible is $a \rightarrow \gamma\gamma$, but at $m_a \geq m_Z$ and $m_a \geq 2m_Z$, the $a \rightarrow \gamma Z$ and $a \rightarrow ZZ$ modes become possible. The corresponding decay widths are

$$\Gamma(a \rightarrow \gamma\gamma) = \frac{4\pi\alpha^2 m_a^3 |C_{\gamma\gamma}|^2}{\Lambda^2}, \quad \Gamma(a \rightarrow \gamma Z) = \frac{8\pi\alpha^2 m_a^3 |C_{\gamma Z}|^2}{s_w^2 c_w^2 \Lambda^2} \left(1 - \frac{m_Z^2}{m_a^2}\right)^3, \\ \Gamma(a \rightarrow ZZ) = \frac{4\pi\alpha^2 m_a^3 |C_{ZZ}|^2}{s_w^4 c_w^4 \Lambda^2} \left(1 - \frac{4m_Z^2}{m_a^2}\right)^{3/2}, \quad (2.7)$$

and the total decay width is $\Gamma_{\text{tot}} = \Gamma(a \rightarrow \gamma\gamma) + \Gamma(a \rightarrow \gamma Z) + \Gamma(a \rightarrow ZZ)$ [14]. The branching ratios (B) for the possible decay modes in our effective benchmark are shown in Figure 1 for $C_{BB} = 1$ and $C_{WW} = 0$. For the entire mass range considered in the primary result of this study, the $a \rightarrow \gamma\gamma$ decay mode is most probable. In the region of masses/couplings addressed by this analysis, the ALP is dominantly prompt.

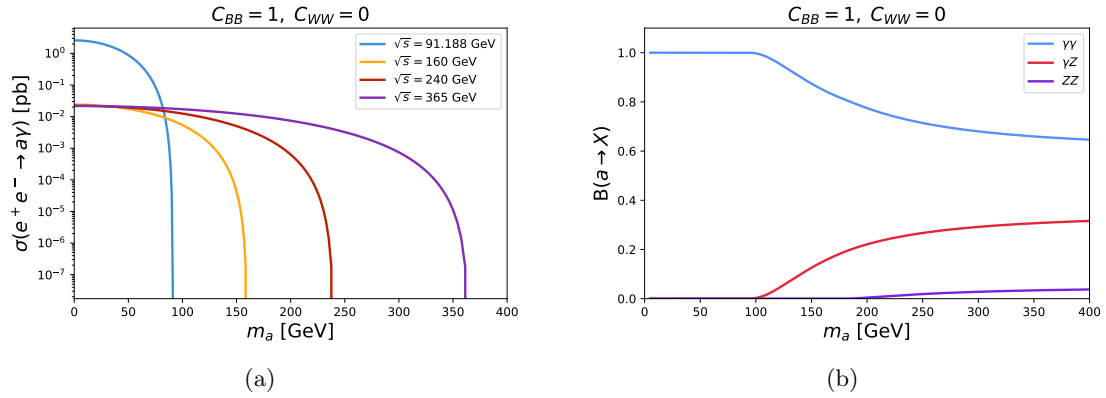


Figure 1. The production cross section of an ALP produced in association with a photon (a), and the branching ratios of possible ALP decay modes (b). The cross sections are in pb for all proposed runs: Z pole (blue), WW threshold (yellow), ZH threshold (red), and $t\bar{t}$ threshold (purple). Possible decay modes in our chosen benchmark scenario are $a \rightarrow \gamma\gamma$ (blue), $a \rightarrow \gamma Z$ (red), and $a \rightarrow ZZ$ (purple).

3 Simulation

The signal process that is simulated is

$$e^+e^- \rightarrow a\gamma, \quad a \rightarrow \gamma\gamma, \quad (3.1)$$

and the Feynman diagram for this process is shown in Figure 2. The most common irreducible background process that yields a 3γ final state is

$$e^+e^- \rightarrow \gamma\gamma\gamma, \quad (3.2)$$

the Feynman diagram for which can also be seen in Figure 2.

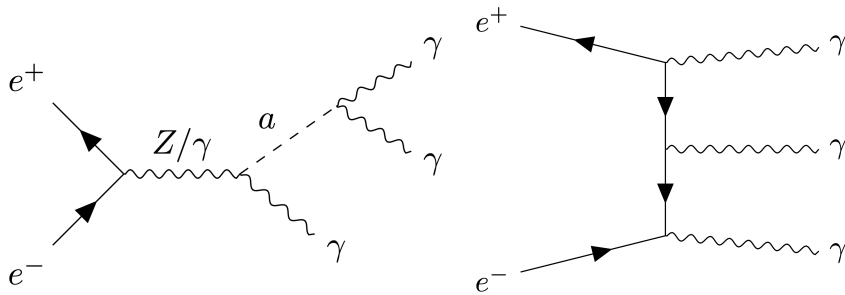


Figure 2. The diagrams for the signal process (left) and background process (right).

3.1 Event simulation

Events are generated for the signal using the Monte Carlo event generator `MG5aMC@NLO` v. 3.6.3 [36] along with the `ALP UFO` v. 1.1 [11] model. All couplings are set to 0 except for

C_{BB} , which is set to 1 and yields

$$C_{\gamma\gamma} = 1, \quad C_{\gamma Z} = -0.223. \quad (3.3)$$

The Λ parameter is set to 1 TeV, and 1 million events are generated for each m_a . The range of m_a probed depends on E_{CM} , and can be found in Table 1. Photons are required to have a minimum energy $E_\gamma > 0.1$ GeV and a maximum pseudorapidity $\eta < 2.6$ at the generation level.

Pole/threshold	E_{CM} [GeV]	m_a range [GeV]	Integrated luminosity [ab^{-1}]
Z	91	5–80	205
WW	160	5–150	19.2
ZH	240	5–220	10.8
$t\bar{t}$	365	5–320	2.7

Table 1. Information about all runs and simulated m_a ranges, with integrated luminosities for each run taken from Ref. [3].

Showering and hadronization are simulated using PYTHIA8 [37], and a fast detector simulation is performed using Delphes [38]. One of the proposed general-purpose detectors to be installed at the FCC-ee is the Innovative Detector for Electron-positron Accelerators (IDEA) [39]. A high-precision vertex detector coupled with a high-granularity calorimeter will lead to high-resolution energy measurements, and the detector will have very good particle identification. In particular, the calorimeter system is comprised of a crystal electromagnetic calorimeter combined with a dual-readout scintillator/fiber hadronic calorimeter [40]. The official IDEA datacard in the “Winter2023” production [41] of the FCC-PED study is used in the Delphes simulation. In the final step, the events are analyzed within the FCCAnalyses framework [42]. Since the current analysis depends on the simulation of the electromagnetic calorimeter, the photon energy resolution is adjusted to reflect the predicted performance specified by the IDEA detector. For an energy E in GeV, the photon resolution is defined as

$$\sigma(E) = \sqrt{0.005^2 E^2 + 0.03^2 E + 0.002^2} \quad (3.4)$$

in the Delphes IDEA card. Photon reconstruction is performed using the default Delphes IDEA card, so the photons are required to have an energy $E \geq 2$ GeV and a $|\eta| \leq 3$ at reconstruction level.

The 3γ background samples are also generated using MG5aMC@NLO v. 3.6.3, using the default SM model input. Showering is simulated with PYTHIA8, and a fast detector simulation is done with Delphes. Analysis is done with FCCAnalyses. Approximately 1 million events are generated at each E_{CM} .

4 Event selection

The first step in the analysis is to correctly assign which photons come from the decay of the ALP (denoted γ_1 and γ_2 , with $E_{\gamma_1} > E_{\gamma_2}$), and which one is produced in association

with the ALP (denoted γ_r). According to the recoil formula, the photon produced in association with the ALP will have an energy of

$$E_r = \frac{E_{CM}^2 - m_a^2}{2E_{CM}}. \quad (4.1)$$

We then define a variable [33]

$$M_{cut}^2 = \frac{(m_{\gamma_1\gamma_2} - m_a)^2}{\sigma(m_a)^2} + \frac{(E_{\gamma_r} - E_r)^2}{\sigma(E_r)^2}, \quad (4.2)$$

where $\sigma(E_r)$ is the photon energy resolution, and $\sigma(m_a)$ is the ALP mass resolution. We iterate over all possible assignments of the three photons in the final state and choose the photon assignment that minimizes M_{cut}^2 . This choice is the best identification given the expected kinematics of the ALP and corresponding recoil photon. The minimum M_{cut} is shown in Figure 3 for two benchmark points $m_a = 100$ and 300 GeV at the $t\bar{t}$ threshold. For the signal, the minimum M_{cut}^2 peaks at a low value, while for the background, there is no peak. The signal and background distributions are rather independent of m_a , and the behavior is similar across all E_{CM} .

Given the same generated background, different photons will be chosen as ALP decay products depending on the ALP mass point. Thus, each ALP mass point yields its own analysis; there are different selection criteria for each mass point, and the overall result is mass-dependent.

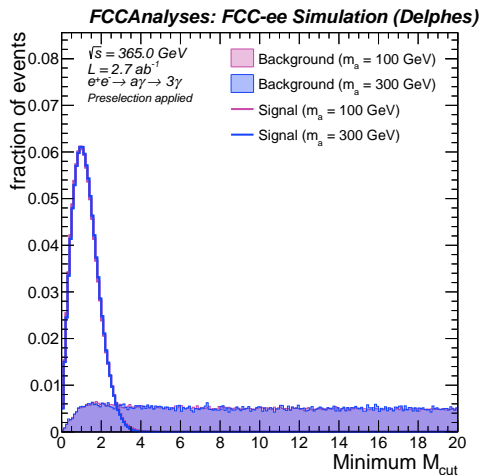


Figure 3. The minimum M_{cut} distribution in the correct photon assignment after preselection at the $t\bar{t}$ threshold for $m_a = 100$ GeV (pink), and 300 GeV (blue). The solid lines correspond to signal samples, while the shaded regions correspond to background samples. The number of events for each distribution is normalized to unity.

4.1 Preselection

The selections are done in two stages: preselection and final selection. The purpose of the preselection is to clean up the events by choosing only those in which the three photons

correspond to the collision, and they can all be resolved. The same preselection is applied to all ALP mass points, but the final selection is optimized for each mass point individually. The effect of the preselection is shown in Table 3, which lists signal efficiency and background rejection values for each center-of-mass energy and m_a value. Typically, about 90% of the signal is kept, and almost 50% of the $e^+e^- \rightarrow \gamma\gamma\gamma$ background is rejected. This preselection also suppresses potential background processes involving Higgs boson or Z boson decays to two photons to a negligible level.

The following selections are applied as a preselection:

- The number of reconstructed photons is required to be exactly three, in order to remove possible backgrounds. Photons are required to have $E \geq 2$ GeV and $|\eta| \leq 3$, and are assigned according to the corresponding ALP kinematics, as described above.
- The invariant mass of the three photons is required to be near $E_{CM} \pm \sigma(m_{\gamma\gamma\gamma})$. The resolution $\sigma(m_{\gamma\gamma\gamma})$ depends on the E_{CM} and can be calculated from the simulation. The values of $\sigma(m_{\gamma\gamma\gamma})$ used in this study are 1.3 GeV (Z pole run), 2.1 GeV (WW threshold), 3.0 GeV (ZH threshold), and 4.2 GeV ($t\bar{t}$ threshold). This requirement is meant to remove any instrumental background, in which a particle may have escaped the detector, or a photon was mis-reconstructed.
- The 3D opening angle between the ALP decay products ($\Delta\alpha_{\gamma_1\gamma_2}$) must be larger than 0.02. This selection is applied to make sure that all photons are properly resolved in the detector [33].

4.2 Final selection

As shown in section 4, the three final-state photons are assigned according to the expected kinematics of the collision. The signal is a sequence of two-body decays, which means that each event is fully defined by five variables: the reconstructed ALP mass ($m_{\gamma_1\gamma_2}$), the $\cos\theta$ and ϕ of the recoil photon in the lab frame, and the $\cos\theta$ and ϕ of one of the ALP decay products in the rest frame of the ALP. The system has cylindrical symmetry around the beam axis, so all of the events are rotated such that $\phi_{\gamma_r} = 0$. Then, the following variables are used to select events, all of which are shown in Figure 4 for the $t\bar{t}$ threshold:

- Minimum M_{cut} (defined in Section 4)
- $\cos\theta_{\gamma_1}$ (calculated in the ALP rest frame)
- ϕ_{γ_1} (calculated in the ALP rest frame)
- $\Delta\alpha_{\gamma_1\gamma_2}$ (the 3D opening angle between the ALP decay products).

The final selection criteria applied to these four variables are determined by maximizing the significance as defined in Ref. [43]. The selection criteria and cutflow tables for all ALP mass points and E_{CM} are provided in the Appendix. The distributions behave in a similar way at the different center-of-mass energies, so only the $t\bar{t}$ threshold is shown here. For example, a benchmark point of $m_a = 25$ GeV at the Z pole behaves similarly

to a benchmark point of $m_a = 100$ GeV at the $t\bar{t}$ threshold, as both of these points have $m_a/E_{CM} \approx 0.27$.

The event normalization is sample-dependent. In the case of signal at the Z pole run, the Z boson propagator receives an enhancement factor (m_Z^2/Γ_Z^2) ≈ 1336 [10], so the events are normalized to the expected number of Z bosons at the FCC-ee Z pole run, 6×10^{12} Z bosons¹. In the case of background at the Z pole run, as well as signal and background for all other proposed FCC-ee runs, the events are normalized to the respective cross sections and integrated luminosities, the former (latter) of which can be found in Table 2 (Table 1).

Since a is a scalar, $|\cos\theta_{\gamma_1}|$ and $|\phi_{\gamma_1}|$ are flat for the signal, while they peak around 1 and $\pi/2$, for the background, respectively. The 3D opening angle $\Delta\alpha_{\gamma_1\gamma_2}$ depends on m_a . At small m_a , the ALP is boosted, and the decay products are collimated, so the angle between γ_1 and γ_2 is close to 0. As the ALP mass increases, the ALP becomes less boosted, and thus the decay products are less collimated. When m_a is very near to the E_{CM} , the angle between γ_1 and γ_2 is very close to π .

The behavior of $|\cos\theta_{\gamma_1}|$ is similar across all m_a for the signal, but not for the background, since the photon assignment is based on the desired ALP kinematics. The same reasoning can be applied to the background samples regarding the $|\phi_{\gamma_1}|$ and $\Delta\alpha_{\gamma_1\gamma_2}$ variables. The signal samples do not behave the same way across all m_a for $\Delta\alpha_{\gamma_1\gamma_2}$ (see above), or for $|\phi_{\gamma_1}|$.

5 Results

In section 5.1, primary results are presented for the $C_{BB} = 1$ benchmark scenario. The results are recast to study the relationship between C_{WW}/C_{BB} in section 5.2.

5.1 Primary results

The expected number of events for all runs, after the full event selection is applied, is shown in Tables 4-7. The expected sensitivity is then computed with these event yields. The statistical analysis is performed with the CMS COMBINE statistical tool [44], based on the ROOFIT [45] and ROOSTATS [46] frameworks. A binned likelihood fit is carried out using the $|\cos\theta_{\gamma_r}|$ distribution as input, as shown in Figure 5 for the $t\bar{t}$ threshold. The distributions behave in a similar way at the different center-of-mass energies, so we choose to show only the $t\bar{t}$ threshold case here. The signal distributions are relatively flat, while the background distributions peak around 1. Limits on the expected signal exclusion are derived using the modified frequentist CL_s criterion [47, 48], with the profile likelihood ratio as the test statistic [49]. The asymptotic approximation to the profile likelihood test statistic [49] is used.

¹The Z pole run will be spread over three separate energies with various integrated luminosities, so the practical recommendation is to normalize the number of events to the expected number of Z bosons (6×10^{12}), rather than to the overall expected integrated luminosity (205 ab^{-1}). Effectively, this is done by first normalizing the number of events to 205 ab^{-1} , and then multiplying by a factor of 0.49. This factor corresponds to the expected number of Z bosons produced at an integrated luminosity of 205 ab^{-1} , compared to the expected number of Z bosons produced during the entirety of the FCC-ee Z pole run.

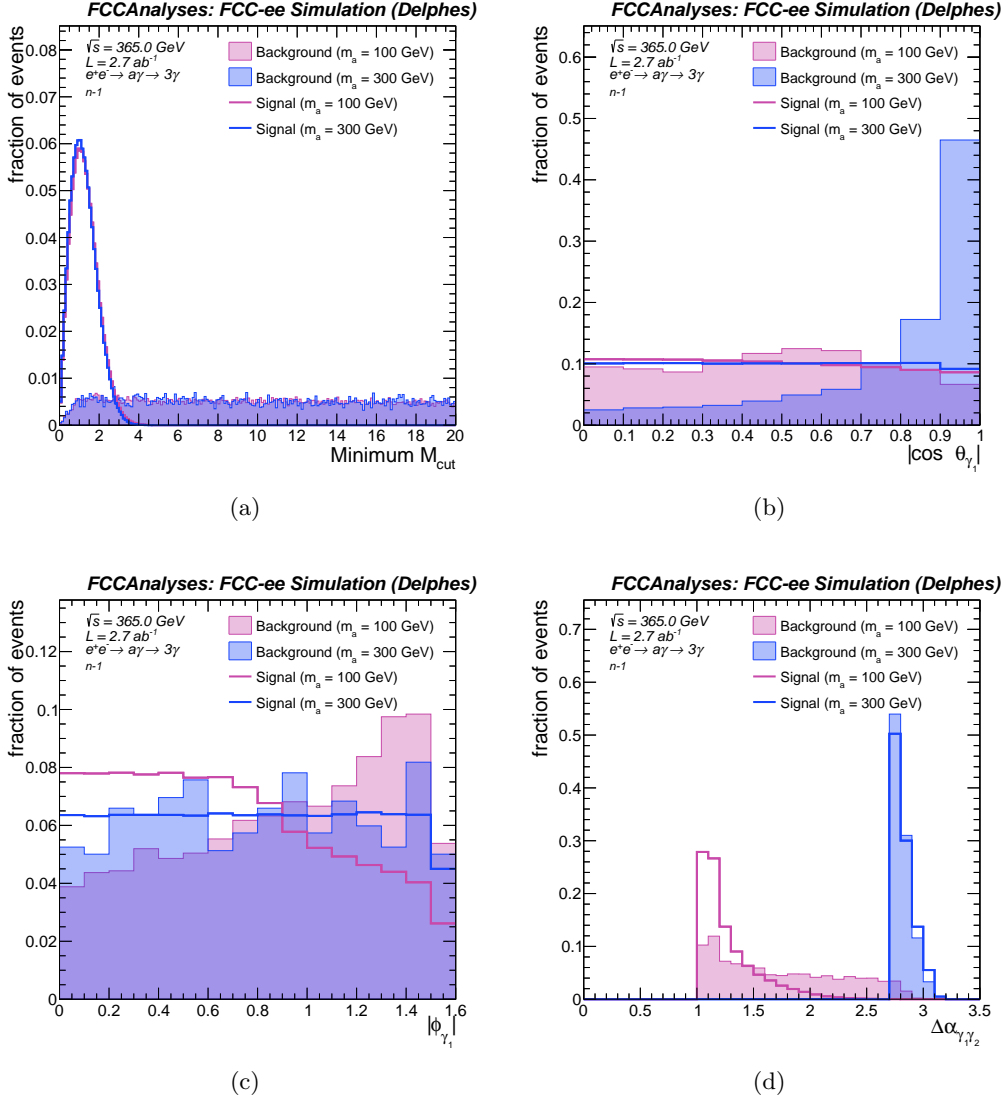


Figure 4. The discriminant variables used in the final event selection at the $t\bar{t}$ threshold for $m_a = 100$ GeV (pink), and 300 GeV (blue). These include M_{cut} (a), $|\cos \theta_{\gamma_1}|$ (b), $|\phi_{\gamma_1}|$ (c), and $\Delta\alpha_{\gamma_1\gamma_2}$ (d). The solid lines correspond to signal samples, while the shaded regions correspond to background samples. The final selection is applied to all variables except the criterion on the variable that is plotted, and the number of events for each distribution is normalized to unity.

The output of this procedure is the sensitivity to the signal strength parameter μ , which is the ratio between the theoretical cross section and the cross section limit: $\mu = \sigma_{lim}/\sigma_{theory}$. The cross section is proportional to $C_{\gamma Z}^2$, which is proportional to $C_{\gamma\gamma}^2$ in our benchmark scenario. The limit on the coupling is found via

$$C_{\gamma\gamma,lim} = C_{\gamma\gamma,theory} \sqrt{\frac{\sigma_{lim}}{\sigma_{theory}}}, \quad (5.1)$$

where $C_{\gamma\gamma,theory}$ and σ_{theory} correspond to our $C_{\gamma\gamma} = 1$ benchmark scenario. The limits

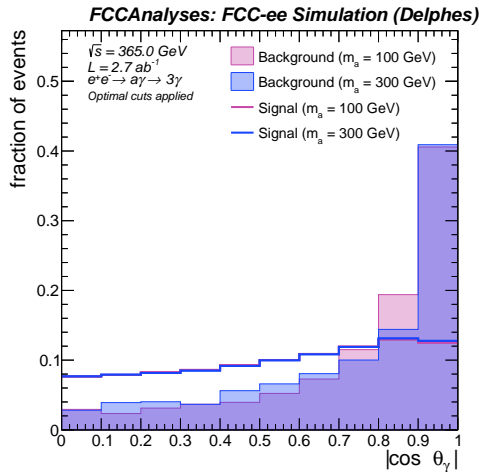


Figure 5. The $|\cos \theta_{\gamma_r}|$ distribution at the $t\bar{t}$ threshold after final selection for $m_a = 100$ GeV (pink), and 300 GeV (blue). The solid lines correspond to signal samples, while the shaded regions correspond to background samples. The number of events for each distribution is normalized to unity.

are shown in terms of $g_{a\gamma\gamma}$, following the current reference reach plots for the ALP photon coupling [32], and current ALP photon coupling exclusions set by previous experiments [50]. The conversion from $C_{\gamma\gamma}$ to $g_{a\gamma\gamma}$ is performed with the equation

$$g_{a\gamma\gamma} = 4e^2 \cdot \frac{C_{\gamma\gamma}}{\Lambda}, \quad (5.2)$$

where $C_{\gamma\gamma} = C_{\gamma\gamma,lim}$, and $\Lambda = 1$ TeV.

The 95% confidence level (CL) projected sensitivity of the FCC-ee to $g_{a\gamma\gamma}$ is shown in Figure 6 at each proposed FCC-ee run, as well as the combined sensitivity over all runs. Below ALP masses of 100 GeV, the best sensitivity is at the Z pole run, with the coupling reaching to 10^{-5} GeV $^{-1}$. The sensitivity at the other runs will be an order of magnitude less, but they probe larger m_a . In the 80 to 150 GeV mass range, multiple runs contribute to the sensitivity. Combining data from different collision energies improves the sensitivity to $g_{a\gamma\gamma}$ by up to a factor of 1.6, depending on the mass, relative to each individual run.

The results from this study can be found in Figure 7, along with previous results from Ref. [33, 34], and already excluded regions of parameter space. In particular, the combined limit from the 3γ final state significantly enhances the current LHC limits when m_a is 90 to 300 GeV. The $\gamma\gamma$ -fusion ALP production mode ($\gamma\gamma \rightarrow a \rightarrow \gamma\gamma$) results obtained from Ref. [34] have better sensitivity in this mass region, and are combined for all proposed center-of-mass energies. However, these results are sensitive only to $C_{\gamma\gamma}$, and assume $B(a \rightarrow \gamma\gamma) = 1$. In contrast, the 3γ final state is sensitive to both $C_{\gamma\gamma}$ and $C_{\gamma Z}$, and takes into account two additional decay modes. In the case of discovery, the measurement of the cross section of ALPs from both $\gamma\gamma$ -fusion and the 3γ channel will allow for the possibility to constrain the relative value of the ALP couplings to the $SU(2)$ and $U(1)$ bosons.

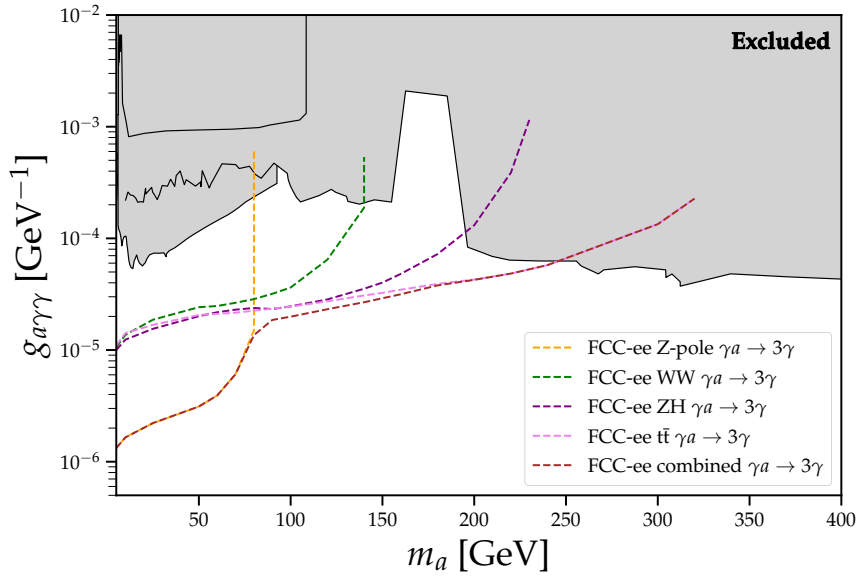


Figure 6. The 95% CL projected sensitivity of the FCC-ee, in the $g_{a\gamma\gamma}$ - m_a plane, from the 3γ final state at the Z pole (yellow), the WW threshold (green), the ZH threshold (purple), the $t\bar{t}$ threshold (pink), and the combined reach of all proposed runs (brown). The grey regions indicate the areas excluded by previous experiments [50].

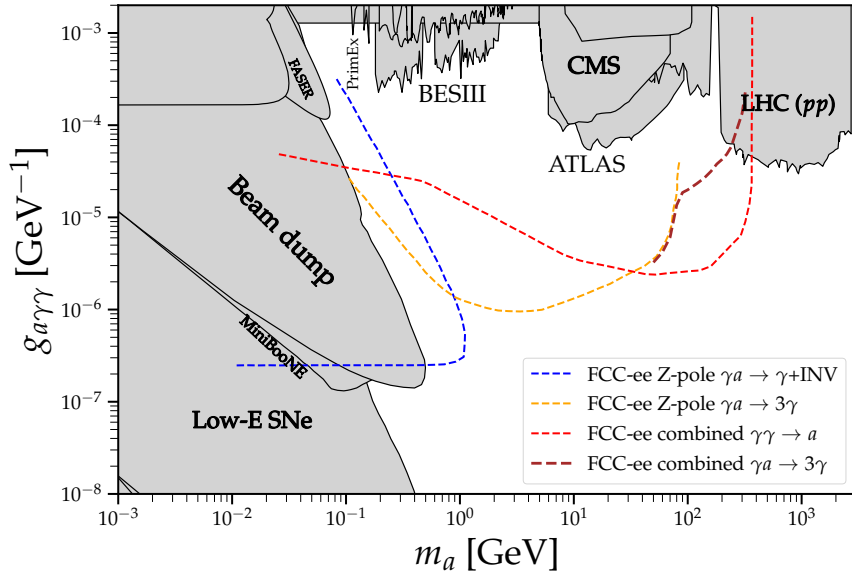


Figure 7. The 95% CL projected sensitivity of the FCC-ee in the $g_{a\gamma\gamma}$ - m_a plane. The brown line indicates the limit for the 3γ final state from this work, for all center-of-mass energies combined. The blue line indicates the monophoton case, when the ALP decays outside of the detector [33]. The yellow line corresponds to the 3γ final state at the Z pole, with special attention given to $0.1 < m_a < 5$ GeV [33]. The red line shows the case where the ALP is produced via $\gamma\gamma$ -fusion [34], for all center-of-mass energies combined. The grey regions indicate the areas excluded by previous experiments [50].

5.2 Dependence of results on Wilson coefficients in Lagrangian

The results for the 3γ final state are obtained for the benchmark scenario where $C_{BB} = 1$ and $C_{WW} = 0$, and they assume only tree-level couplings. Below the Z -mass, this corresponds to a situation where $B(a \rightarrow \gamma\gamma)$ is 1, and the cross section is determined predominantly by the $C_{\gamma Z}$ coupling, which is related to $C_{\gamma\gamma}$ by the equation $C_{\gamma Z} = -s_w^2 C_{\gamma\gamma}$. The situation becomes more complex for different center-of-mass energies, where the cross section depends on both $C_{\gamma\gamma}$ and $C_{\gamma Z}$, and the additional decays into γZ , WW , and ZZ progressively open up. In literature (for instance Ref. [51]), different proposals of UV-complete models are found for which the choice of C_{BB} and C_{WW} is different from the benchmark adopted for this study. It is therefore interesting to understand the FCC-ee potential for measuring C_{BB} and C_{WW} separately. The present analysis is recast for different choices of $r \equiv C_{WW}/C_{BB}$, varying between -1.5 and 1.5, and these results are shown in Figures 8 and 9. The 3γ production is enhanced by the increase in $C_{\gamma Z}$ for $r < 0$ and $r > 0.9$, yielding a large gain in sensitivity for $m_a < m_Z$. The gain in sensitivity increases as one approaches the configuration $C_{WW} = -C_{BB}$, corresponding to the photophobic case described in Ref. [51]. The 3γ production is decreased by the decrease in $C_{\gamma Z}$ for r values between 0 and 0.9, with the largest dip in sensitivity corresponding to $r \approx 0.3$. For $m_a > m_Z$, the rise in $C_{\gamma Z}$ is compensated on one hand by the decrease in $C_{\gamma\gamma}$, and on the other hand by the fact that $B(a \rightarrow \gamma\gamma)$ becomes smaller than 1 because different decay channels open up. The final result is that for $m_a > m_Z$, the sensitive area is approximately insensitive to the value of r . However, in this mass region, dedicated searches for the decay into γZ , WW , and ZZ would provide an additional measurement in case of discovery, thus constraining C_{BB} and C_{WW} . The change in sensitivity as a function of r is shown for three different ALP masses in Figure 10. The decay modes that we consider are $\gamma\gamma$, γZ , and ZZ , so we choose to look at one benchmark mass $m_a < m_Z$, a second benchmark mass $m_Z < m_a < 2m_Z$, and a benchmark mass $m_a > 2m_Z$. For $m_a < m_Z$, the results are sensitive to the value of r and the variation in sensitivity spans many orders of magnitude. At $r = 0.3$, the drastic loss in sensitivity can be understood from Eq. 2.2. At approximately this point, $C_{\gamma Z}$ is 0 and production of the 3γ final state occurs entirely via photon exchange, whose contribution is small at the Z pole run, but dominant at the other center-of-mass energies. This accounts for the difference in the variation in reach at the Z pole run compared to the $t\bar{t}$ threshold results or the combined results. However, for $m_a > m_Z$, the variation in reach is at most a factor of 2 over the range of r considered.

Over the whole mass range of interest, two different production processes are available: the one studied in this paper and $\gamma\gamma$ fusion. A complete study of how the two measurements may be combined would require a complete recast of the results of Ref. [34], which are based on an effective Lagrangian with only the $C_{\gamma\gamma}$ coupling. For $m_a < m_Z$, this is a good approximation of the Lagrangian in Eq. (2.1), as the only relevant production and decay processes go through $C_{\gamma\gamma}$, and thus the sensitivity in terms of $C_{\gamma\gamma}$, shown in Figures 8 and 9 as a red dashed line, does not depend on the value of r . For $m_a > m_Z$ and this Lagrangian, $\gamma\gamma$ fusion is supplemented by γZ , WW , and ZZ fusion, and the branching fraction for the decay into two photons will be suppressed as for the 3γ channel. A complete recalculation

of the FCC-ee sensitivity to VBF fusion based on this Lagrangian is outside the scope of this paper, but it should be pursued in the future. Similarly, the model dependence of the existing limits should be evaluated.

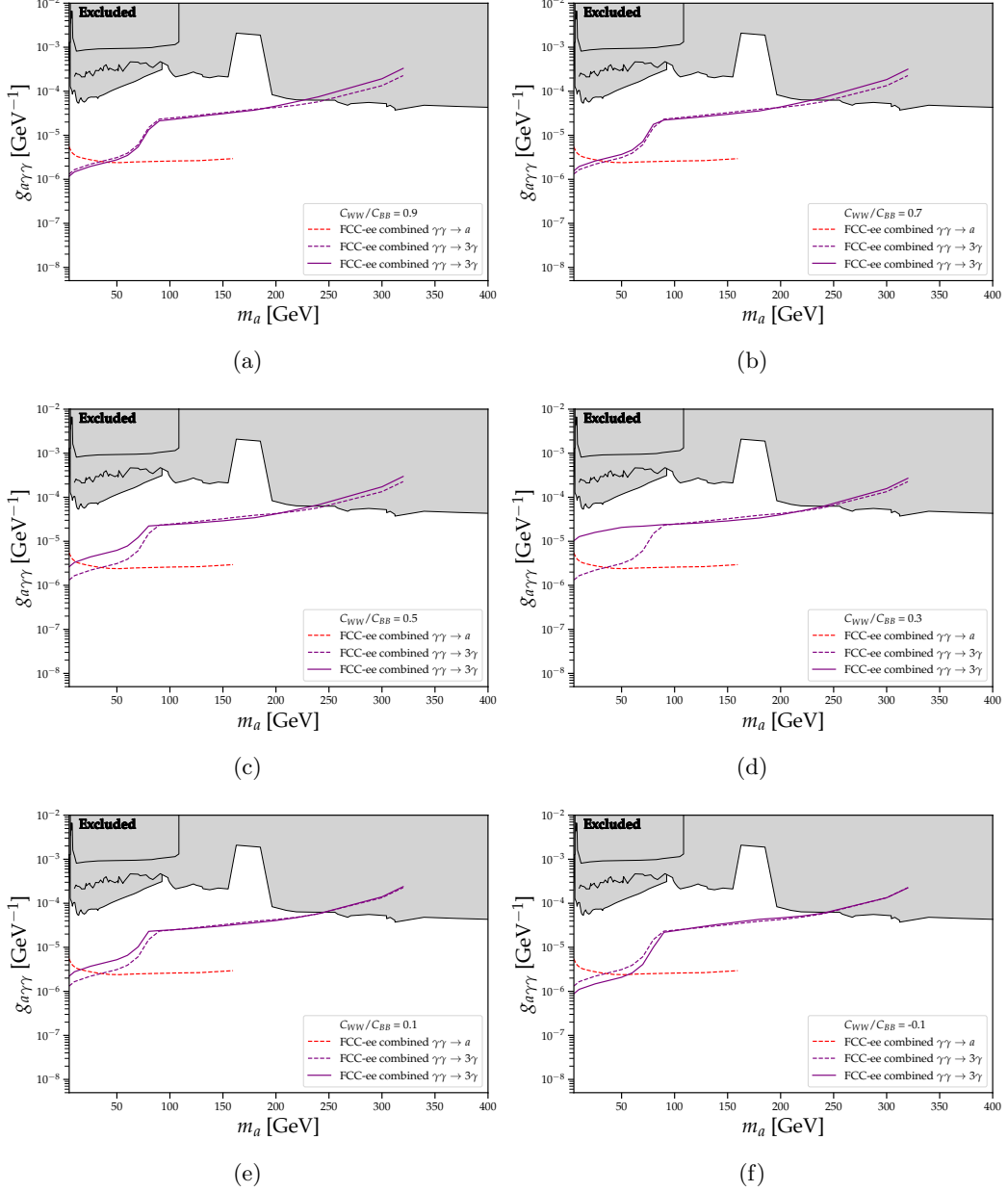


Figure 8. The 95% CL projected sensitivity of the FCC-ee in the $g_{a\gamma\gamma}$ - m_a plane, for all center-of-mass energies combined. Plots a-f correspond to decreasing C_{WW}/C_{BB} values from 0.9 to -0.1. The dashed purple line indicates the primary 3γ result, and the solid purple line corresponds to the recast 3γ result for the listed C_{WW}/C_{BB} value. At each mass point, the center-of-mass energy with the best limit is taken for the combined lines. The dashed red line indicates the $\gamma\gamma$ -fusion [34] result, for $m_a < m_Z$. The grey regions indicate the areas excluded by previous experiments [50], and are not altered.

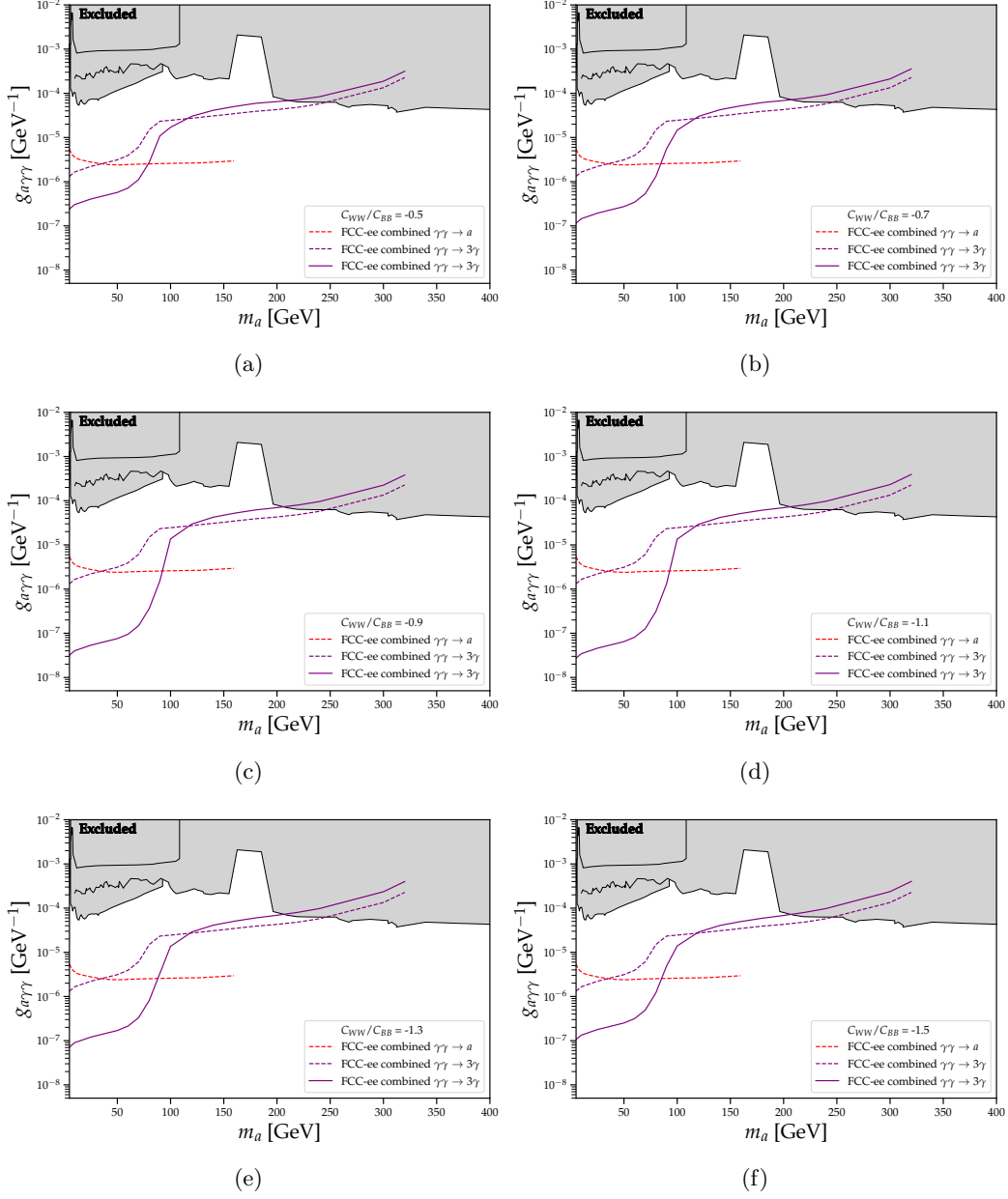


Figure 9. The 95% CL projected sensitivity of the FCC-ee in the $g_{a\gamma\gamma}$ - m_a plane, for all center-of-mass energies combined. Plots a-f correspond to decreasing C_{WW}/C_{BB} values from -0.5 to -1.5. The dashed purple line indicates the primary 3γ result, and the solid purple line corresponds to the recast 3γ result for the listed C_{WW}/C_{BB} value. At each mass point, the center-of-mass energy with the best limit is taken for the combined lines. The dashed red line indicates the $\gamma\gamma$ -fusion [34] result, for $m_a < m_Z$. The grey regions indicate the areas excluded by previous experiments [50], and are not altered.

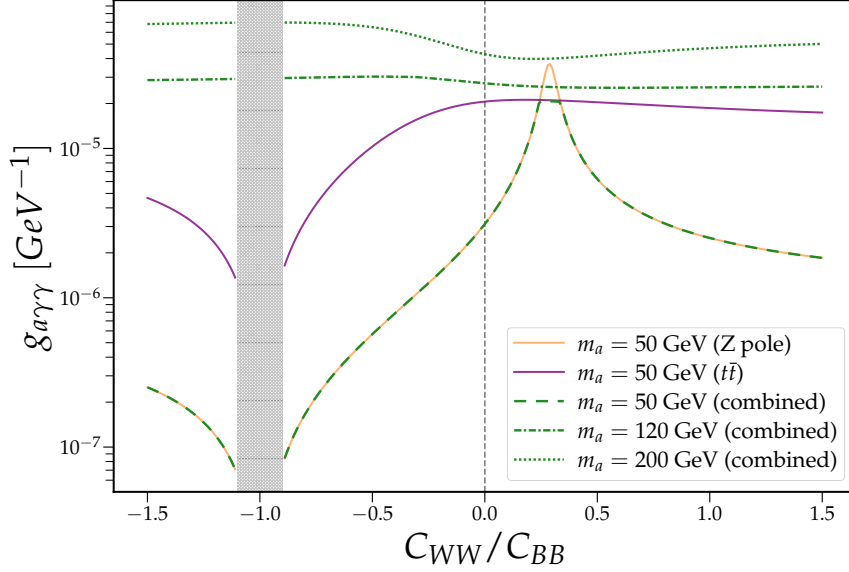


Figure 10. The 95% CL projected sensitivity of the FCC-ee as a function of $r \equiv C_{WW}/C_{BB}$. The yellow line corresponds to the $m_a = 50$ GeV results at the Z pole run, and the purple line corresponds to the $m_a = 50$ GeV results at the $t\bar{t}$ threshold. The dashed green line corresponds to the combined $m_a = 50$ GeV results. The dash-dotted green line corresponds to the combined $m_a = 120$ GeV results, and the dotted green line corresponds to the combined $m_a = 200$ GeV results. At each r value, the center-of-mass energy with the best limit is taken for the combined lines. The dashed grey line is the primary result in this study. At the photophobic case $C_{WW} = -C_{BB}$, there is zero sensitivity to the signal, and near this point, radiative corrections become important. For this reason, the $r = -0.9$ and $r = -1.1$ results are not connected, and the region in between is shaded. At these values of r , the corrections are negligible.

6 Summary and outlook

We have presented a feasibility study on the observation of axion-like particles (ALPs) at the FCC-ee, a planned future e^+e^- collider. The ALP is produced in association with a photon and decays to two photons, $e^+e^- \rightarrow a\gamma \rightarrow 3\gamma$. The process is simulated using the IDEA detector configuration at all proposed FCC-ee runs: the Z pole run, WW threshold, ZH threshold, and $t\bar{t}$ threshold. Event selection criteria are applied to optimize the significance, and sensitivity projections are made for all runs separately, as well as all runs combined. As expected, the Z pole run probes the smallest couplings due to the expected high luminosity. In contrast, the higher center-of-mass energy runs can probe larger ALP masses, specifically from around 90 to 320 GeV. The sensitivity of all runs combined is improved with respect to the individual FCC-ee runs for masses between 80 and 150 GeV. For masses between 90 and 300 GeV, the 3γ photon final state results extend the current LHC limits. The overall result is mass-dependent; in the future, once the FCC collects data, the analysis will be performed with different categories of m_a and different selections per category. Overall, this study shows that there is good potential to explore the ALP phase space at the FCC-ee by extending to higher center-of-mass energy runs.

The FCC-ee can also measure C_{WW} and C_{BB} separately when the 3γ and 2γ modes are measured independently. The 3γ production is sensitive to the value of $r \equiv C_{WW}/C_{BB}$ for $m_a < m_Z$, with the largest gain in sensitivity as the photophobic case $C_{WW} = -C_{BB}$ is approached. For $m_a > m_Z$, the result is approximately insensitive to the value of r . For $m_a < m_Z$, comparisons have been made to previous ALP studies at the FCC-ee. In particular, the $\gamma\gamma$ -fusion result is dependent only on $C_{\gamma\gamma}$, while the 3γ final state is sensitive also to $C_{\gamma Z}$, thus it has the ability to measure C_{WW}/C_{BB} . In the higher mass region, additional fusion processes would contribute to production and would also be able to constrain C_{WW} and C_{BB} . In summary, we demonstrate the strong potential of the FCC-ee to probe and distinguish the underlying electroweak structure of ALP couplings.

Acknowledgments

JA, EB, FB, JDA, CD, JN, AP, and LR acknowledge support from DESY (Hamburg, Germany), a member of the Helmholtz Association HGF, and support by the Deutsche Forschungsgemeinschaft (DFG, German Research Foundation) under Germany's Excellence Strategy – EXC 2121 "Quantum Universe" – 390833306. JDA acknowledges partial support from the Egyptian governmental funding agency, Science, Technology & Innovation Funding Authority (STDF) (Grant No. 50806).

A Appendix

This appendix contains tables with detailed information regarding the event normalization and selection. There is a table that contains the cross sections used to normalize the number of signal events. Another table contains the values for signal efficiency and background rejection for each selection stage. The rest of the tables contain detailed information on the event selection at each center-of-mass energy, as well as the number of events after the preselection and final selection, for all FCC-ee runs.

m_a [GeV]	$\sigma(e^+e^- \rightarrow \gamma a)$ [pb]			
	Z pole	WW	ZH	$t\bar{t}$
5	2.4×10^0	2.2×10^{-2}	2.0×10^{-2}	2.0×10^{-2}
10	2.4×10^0	2.2×10^{-2}	2.0×10^{-2}	2.0×10^{-2}
25	2.0×10^0	2.0×10^{-2}	2.0×10^{-2}	2.0×10^{-2}
50	8.5×10^{-1}	1.6×10^{-2}	1.8×10^{-2}	1.9×10^{-2}
60	4.5×10^{-1}	1.4×10^{-2}	1.7×10^{-2}	1.9×10^{-2}
70	1.7×10^{-1}	1.2×10^{-2}	1.6×10^{-2}	1.8×10^{-2}
80	3.0×10^{-2}	9.2×10^{-3}	1.4×10^{-2}	1.7×10^{-2}
90	—	7.0×10^{-3}	1.3×10^{-2}	1.7×10^{-2}
100	—	4.9×10^{-3}	1.2×10^{-2}	1.6×10^{-2}
120	—	1.7×10^{-3}	8.3×10^{-3}	1.4×10^{-2}
140	—	2.5×10^{-4}	5.3×10^{-3}	1.1×10^{-2}
150	—	3.4×10^{-5}	4.1×10^{-3}	1.0×10^{-2}
160	—	—	3.0×10^{-3}	9.1×10^{-3}
180	—	—	1.4×10^{-3}	7.1×10^{-3}
200	—	—	4.5×10^{-4}	5.4×10^{-3}
220	—	—	6.2×10^{-5}	3.9×10^{-3}
240	—	—	—	2.7×10^{-3}
300	—	—	—	4.7×10^{-4}
320	—	—	—	1.7×10^{-4}

Table 2. The ALP production cross section for each mass point and center-of-mass energy. The cross sections are computed with MG5aMC@NLO v. 3.6.3.

m_a [GeV]		After preselection				After final selection			
		Z pole	WW	ZH	$t\bar{t}$	Z pole	WW	ZH	$t\bar{t}$
5	S efficiency	0.827	0.887	0.903	0.914	0.504	0.563	0.402	0.651
	B rejection	0.536	0.484	0.453	0.423	0.997	0.998	0.999	0.998
10	S efficiency	0.830	0.879	0.894	0.879	0.516	0.413	0.409	0.645
	B rejection	0.536	0.484	0.453	0.423	0.996	0.998	0.999	0.997
25	S efficiency	0.875	0.902	0.894	0.895	0.494	0.484	0.550	0.547
	B rejection	0.536	0.484	0.453	0.423	0.997	0.997	0.996	0.997
50	S efficiency	0.874	0.900	0.900	0.901	0.535	0.518	0.497	0.451
	B rejection	0.536	0.484	0.453	0.423	0.998	0.998	0.997	0.998
60	S efficiency	0.874	0.901	0.900	0.901	0.537	0.450	0.472	0.518
	B rejection	0.536	0.484	0.453	0.423	0.999	0.998	0.998	0.997
70	S efficiency	0.875	0.901	0.900	0.901	0.537	0.477	0.421	0.549
	B rejection	0.536	0.484	0.453	0.423	0.999	0.998	0.998	0.998
80	S efficiency	0.877	0.902	0.900	0.900	0.539	0.552	0.434	0.480
	B rejection	0.536	0.484	0.453	0.423	0.998	0.998	0.998	0.998
90	S efficiency	—	0.901	0.900	0.900	—	0.472	0.448	0.468
	B rejection	—	0.484	0.453	0.423	—	0.999	0.999	0.998
100	S efficiency	—	0.902	0.901	0.900	—	0.553	0.433	0.499
	B rejection	—	0.484	0.453	0.423	—	0.999	0.999	0.998
120	S efficiency	—	0.901	0.901	0.901	—	0.554	0.551	0.555
	B rejection	—	0.484	0.453	0.423	—	0.999	0.998	0.998
140	S efficiency	—	0.900	0.901	0.900	—	0.555	0.549	0.561
	B rejection	—	0.484	0.453	0.423	—	0.999	0.999	0.998
150	S efficiency	—	0.902	0.901	0.901	—	0.555	0.535	0.506
	B rejection	—	0.484	0.452	0.423	—	0.998	0.999	0.998
160	S efficiency	—	—	0.902	0.901	—	—	0.553	0.513
	B rejection	—	—	0.453	0.423	—	—	0.999	0.998
180	S efficiency	—	—	0.902	0.901	—	—	0.474	0.552
	B rejection	—	—	0.453	0.423	—	—	0.999	0.998
200	S efficiency	—	—	0.901	0.901	—	—	0.554	0.551
	B rejection	—	—	0.453	0.423	—	—	0.999	0.999
220	S efficiency	—	—	0.902	0.901	—	—	0.555	0.552
	B rejection	—	—	0.453	0.423	—	—	0.999	0.999
240	S efficiency	—	—	—	0.901	—	—	—	0.553
	B rejection	—	—	—	0.423	—	—	—	0.999
300	S efficiency	—	—	—	0.901	—	—	—	0.552
	B rejection	—	—	—	0.423	—	—	—	0.999
320	S efficiency	—	—	—	0.901	—	—	—	0.550
	B rejection	—	—	—	0.423	—	—	—	0.999

Table 3. The signal (S) efficiency and background (B) rejection is shown, for each mass point. The first two columns correspond to m_a and S efficiency/B rejection. The next four columns correspond to the various center-of-mass energies studied, with values after the preselection is applied. The last four columns correspond to the various center-of-mass energies once the final selection is applied.

Z pole run

m_a [GeV]	M_{cut}	$ \cos \theta_{\gamma_1} $	$ \phi_{\gamma_1} $	$\Delta\alpha_{\gamma_1\gamma_2}$		No selection	Preselection	Final selection
5	<2.0	<1.0	<1.6	<0.3	S	$2.5 \times 10^8 \pm 2.5 \times 10^5$	$2.0 \times 10^8 \pm 2.2 \times 10^5$	$1.2 \times 10^8 \pm 1.7 \times 10^5$
					B	$1.8 \times 10^9 \pm 1.8 \times 10^6$	$8.6 \times 10^8 \pm 1.3 \times 10^6$	$5.2 \times 10^6 \pm 9.8 \times 10^4$
10	<2.0	<1.0	<1.6	<0.6	S	$2.4 \times 10^8 \pm 2.4 \times 10^5$	$1.9 \times 10^8 \pm 2.2 \times 10^5$	$1.2 \times 10^8 \pm 1.7 \times 10^5$
					B	$1.8 \times 10^9 \pm 1.8 \times 10^6$	$8.6 \times 10^8 \pm 1.3 \times 10^6$	$8.0 \times 10^6 \pm 1.2 \times 10^5$
25	<2.0	<1.0	<1.2	<1.5	S	$2.0 \times 10^8 \pm 2.0 \times 10^5$	$1.7 \times 10^8 \pm 1.8 \times 10^5$	$9.7 \times 10^7 \pm 1.4 \times 10^5$
					B	$1.8 \times 10^9 \pm 1.8 \times 10^6$	$8.6 \times 10^8 \pm 1.3 \times 10^6$	$5.6 \times 10^6 \pm 1.0 \times 10^5$
50	<2.0	<0.7	<1.6	<3.1	S	$8.5 \times 10^7 \pm 8.5 \times 10^4$	$7.4 \times 10^7 \pm 7.9 \times 10^4$	$4.5 \times 10^7 \pm 6.2 \times 10^4$
					B	$1.8 \times 10^9 \pm 1.8 \times 10^6$	$8.6 \times 10^8 \pm 1.3 \times 10^6$	$3.3 \times 10^6 \pm 7.8 \times 10^4$
60	<2.0	<0.7	<1.6	<3.2	S	$4.5 \times 10^7 \pm 4.5 \times 10^4$	$4.0 \times 10^7 \pm 4.2 \times 10^4$	$2.4 \times 10^7 \pm 3.3 \times 10^4$
					B	$1.8 \times 10^9 \pm 1.8 \times 10^6$	$8.6 \times 10^8 \pm 1.3 \times 10^6$	$2.6 \times 10^6 \pm 7.0 \times 10^4$
70	<2.0	<0.7	<1.6	<3.2	S	$1.7 \times 10^7 \pm 1.7 \times 10^4$	$1.5 \times 10^7 \pm 1.6 \times 10^4$	$9.2 \times 10^6 \pm 1.3 \times 10^4$
					B	$1.8 \times 10^9 \pm 1.8 \times 10^6$	$8.6 \times 10^8 \pm 1.3 \times 10^6$	$2.5 \times 10^6 \pm 6.7 \times 10^4$
80	<2.0	<0.7	<1.6	<3.2	S	$3.0 \times 10^6 \pm 3.0 \times 10^3$	$2.7 \times 10^6 \pm 2.8 \times 10^3$	$1.6 \times 10^6 \pm 2.2 \times 10^3$
					B	$1.8 \times 10^9 \pm 1.8 \times 10^6$	$8.6 \times 10^8 \pm 1.3 \times 10^6$	$2.9 \times 10^6 \pm 7.3 \times 10^4$

Table 4. Event selections at the Z pole, for each mass point. The rightmost columns show the number of events for no applied selection, after the preselection criteria, and after the final selection criteria, for both signal (S) and background (B).

WW threshold

m_a [GeV]	M_{cut}	$ \cos \theta_{\gamma_1} $	$ \phi_{\gamma_1} $	$\Delta\alpha_{\gamma_1\gamma_2}$		No selection	Preselection	Final selection
5	<2.0	<1.0	<1.6	<0.2	S	$4.2 \times 10^5 \pm 4.2 \times 10^2$	$3.7 \times 10^5 \pm 3.9 \times 10^2$	$2.3 \times 10^5 \pm 3.1 \times 10^2$
					B	$5.9 \times 10^7 \pm 5.9 \times 10^4$	$3.1 \times 10^7 \pm 4.3 \times 10^4$	$1.4 \times 10^5 \pm 2.9 \times 10^3$
10	<2.0	<1.0	<1.6	<0.3	S	$4.1 \times 10^5 \pm 4.1 \times 10^2$	$3.6 \times 10^5 \pm 3.9 \times 10^2$	$1.7 \times 10^5 \pm 2.7 \times 10^2$
					B	$5.9 \times 10^7 \pm 5.9 \times 10^4$	$3.1 \times 10^7 \pm 4.3 \times 10^4$	$1.0 \times 10^5 \pm 2.5 \times 10^3$
25	<2.0	<1.0	<1.2	<0.9	S	$3.9 \times 10^5 \pm 3.9 \times 10^2$	$3.5 \times 10^5 \pm 3.7 \times 10^2$	$1.9 \times 10^5 \pm 2.7 \times 10^2$
					B	$5.9 \times 10^7 \pm 5.9 \times 10^4$	$3.1 \times 10^7 \pm 4.3 \times 10^4$	$1.9 \times 10^5 \pm 3.4 \times 10^3$
50	<2.0	<1.0	<1.0	<1.7	S	$3.0 \times 10^5 \pm 3.0 \times 10^2$	$2.8 \times 10^5 \pm 2.9 \times 10^2$	$1.6 \times 10^5 \pm 2.2 \times 10^2$
					B	$5.9 \times 10^7 \pm 5.9 \times 10^4$	$3.1 \times 10^7 \pm 4.3 \times 10^4$	$1.5 \times 10^5 \pm 2.9 \times 10^3$
60	<2.0	<1.0	<1.1	<1.8	S	$2.7 \times 10^5 \pm 2.7 \times 10^2$	$2.4 \times 10^5 \pm 2.5 \times 10^2$	$1.2 \times 10^5 \pm 1.8 \times 10^2$
					B	$5.9 \times 10^7 \pm 5.9 \times 10^4$	$3.1 \times 10^7 \pm 4.3 \times 10^4$	$1.0 \times 10^5 \pm 2.4 \times 10^3$
70	<2.0	<1.0	<1.2	<2.0	S	$2.2 \times 10^5 \pm 2.2 \times 10^2$	$2.0 \times 10^5 \pm 2.1 \times 10^2$	$1.1 \times 10^5 \pm 1.5 \times 10^2$
					B	$5.9 \times 10^7 \pm 5.9 \times 10^4$	$3.1 \times 10^7 \pm 4.3 \times 10^4$	$1.0 \times 10^5 \pm 2.5 \times 10^3$
80	<2.0	<0.7	<1.6	<3.2	S	$1.8 \times 10^5 \pm 1.8 \times 10^2$	$1.6 \times 10^5 \pm 1.7 \times 10^2$	$9.7 \times 10^4 \pm 1.3 \times 10^2$
					B	$5.9 \times 10^7 \pm 5.9 \times 10^4$	$3.1 \times 10^7 \pm 4.3 \times 10^4$	$1.1 \times 10^5 \pm 2.5 \times 10^3$
90	<2.0	<0.6	<1.6	<3.2	S	$1.3 \times 10^5 \pm 1.3 \times 10^2$	$1.2 \times 10^5 \pm 1.3 \times 10^2$	$6.3 \times 10^4 \pm 9.2 \times 10^1$
					B	$5.9 \times 10^7 \pm 5.9 \times 10^4$	$3.1 \times 10^7 \pm 4.3 \times 10^4$	$5.9 \times 10^4 \pm 1.9 \times 10^3$
100	<2.0	<0.7	<1.6	<3.2	S	$9.4 \times 10^4 \pm 9.4 \times 10^1$	$8.5 \times 10^4 \pm 9.0 \times 10^1$	$5.2 \times 10^4 \pm 7.0 \times 10^1$
					B	$5.9 \times 10^7 \pm 5.9 \times 10^4$	$3.1 \times 10^7 \pm 4.3 \times 10^4$	$6.9 \times 10^4 \pm 2.0 \times 10^3$
120	<2.0	<0.7	<1.6	<3.2	S	$3.4 \times 10^4 \pm 3.4 \times 10^1$	$3.0 \times 10^4 \pm 3.2 \times 10^1$	$1.9 \times 10^4 \pm 2.5 \times 10^1$
					B	$5.9 \times 10^7 \pm 5.9 \times 10^4$	$3.1 \times 10^7 \pm 4.3 \times 10^4$	$6.4 \times 10^4 \pm 2.0 \times 10^3$
140	<2.0	<0.7	<1.6	<3.2	S	$4.9 \times 10^3 \pm 4.9 \times 10^0$	$4.4 \times 10^3 \pm 4.6 \times 10^0$	$2.7 \times 10^3 \pm 3.6 \times 10^0$
					B	$5.9 \times 10^7 \pm 5.9 \times 10^4$	$3.1 \times 10^7 \pm 4.3 \times 10^4$	$7.1 \times 10^4 \pm 2.1 \times 10^3$
150	<2.0	<0.7	<1.6	<3.2	S	$6.5 \times 10^2 \pm 6.5 \times 10^{-1}$	$5.9 \times 10^2 \pm 6.2 \times 10^{-1}$	$3.6 \times 10^2 \pm 4.9 \times 10^{-1}$
					B	$5.9 \times 10^7 \pm 5.9 \times 10^4$	$3.1 \times 10^7 \pm 4.3 \times 10^4$	$8.9 \times 10^4 \pm 2.3 \times 10^3$

Table 5. Event selections at the WW threshold, for each mass point. The rightmost columns show the number of events for no applied selection, after the preselection criteria, and after the final selection criteria, for both signal (S) and background (B).

ZH threshold

m_a [GeV]	M_{cut}	$ \cos\theta_{\gamma_1} $	$ \phi_{\gamma_1} $	$\Delta\alpha_{\gamma_1\gamma_2}$		No selection	Preselection	Final selection
5	<2.0	<1.0	<1.6	<0.1	S	$2.2 \times 10^5 \pm 2.2 \times 10^2$	$2.0 \times 10^5 \pm 2.1 \times 10^2$	$8.9 \times 10^4 \pm 1.4 \times 10^2$
					B	$1.5 \times 10^7 \pm 1.5 \times 10^4$	$8.4 \times 10^6 \pm 1.1 \times 10^4$	$1.3 \times 10^4 \pm 4.4 \times 10^2$
10	<2.0	<1.0	<1.6	<0.2	S	$2.2 \times 10^5 \pm 2.2 \times 10^2$	$2.0 \times 10^5 \pm 2.1 \times 10^2$	$9.0 \times 10^4 \pm 1.4 \times 10^2$
					B	$1.5 \times 10^7 \pm 1.5 \times 10^4$	$8.4 \times 10^6 \pm 1.1 \times 10^4$	$2.1 \times 10^4 \pm 5.7 \times 10^2$
25	<2.0	<1.0	<1.6	<0.6	S	$2.1 \times 10^5 \pm 2.1 \times 10^2$	$1.9 \times 10^5 \pm 2.0 \times 10^2$	$1.2 \times 10^5 \pm 1.6 \times 10^2$
					B	$1.5 \times 10^7 \pm 1.5 \times 10^4$	$8.4 \times 10^6 \pm 1.1 \times 10^4$	$6.3 \times 10^4 \pm 9.8 \times 10^2$
50	<2.0	<1.0	<1.2	<1.2	S	$1.9 \times 10^5 \pm 1.9 \times 10^2$	$1.7 \times 10^5 \pm 1.8 \times 10^2$	$9.6 \times 10^4 \pm 1.4 \times 10^2$
					B	$1.5 \times 10^7 \pm 1.5 \times 10^4$	$8.4 \times 10^6 \pm 1.1 \times 10^4$	$4.2 \times 10^4 \pm 8.0 \times 10^2$
60	<2.0	<1.0	<1.1	<1.4	S	$1.8 \times 10^5 \pm 1.8 \times 10^2$	$1.6 \times 10^5 \pm 1.7 \times 10^2$	$8.6 \times 10^4 \pm 1.3 \times 10^2$
					B	$1.5 \times 10^7 \pm 1.5 \times 10^4$	$8.4 \times 10^6 \pm 1.1 \times 10^4$	$3.4 \times 10^4 \pm 7.2 \times 10^2$
70	<2.0	<1.0	<1.0	<1.4	S	$1.7 \times 10^5 \pm 1.7 \times 10^2$	$1.5 \times 10^5 \pm 1.6 \times 10^2$	$7.1 \times 10^4 \pm 1.1 \times 10^2$
					B	$1.5 \times 10^7 \pm 1.5 \times 10^4$	$8.4 \times 10^6 \pm 1.1 \times 10^4$	$2.4 \times 10^4 \pm 6.1 \times 10^2$
80	<2.0	<1.0	<1.0	<1.5	S	$1.5 \times 10^5 \pm 1.5 \times 10^2$	$1.4 \times 10^5 \pm 1.5 \times 10^2$	$6.7 \times 10^4 \pm 1.0 \times 10^2$
					B	$1.5 \times 10^7 \pm 1.5 \times 10^4$	$8.4 \times 10^6 \pm 1.1 \times 10^4$	$2.4 \times 10^4 \pm 6.1 \times 10^2$
90	<2.0	<1.0	<1.1	<1.7	S	$1.4 \times 10^5 \pm 1.4 \times 10^2$	$1.3 \times 10^5 \pm 1.3 \times 10^2$	$6.3 \times 10^4 \pm 9.4 \times 10^1$
					B	$1.5 \times 10^7 \pm 1.5 \times 10^4$	$8.4 \times 10^6 \pm 1.1 \times 10^4$	$2.1 \times 10^4 \pm 5.7 \times 10^2$
100	<2.0	<1.0	<1.1	<1.8	S	$1.2 \times 10^5 \pm 1.2 \times 10^2$	$1.1 \times 10^5 \pm 1.2 \times 10^2$	$5.4 \times 10^4 \pm 8.2 \times 10^1$
					B	$1.5 \times 10^7 \pm 1.5 \times 10^4$	$8.4 \times 10^6 \pm 1.1 \times 10^4$	$1.9 \times 10^4 \pm 5.5 \times 10^2$
120	<2.0	<0.7	<1.6	<1.9	S	$9.0 \times 10^4 \pm 9.0 \times 10^1$	$8.1 \times 10^4 \pm 8.5 \times 10^1$	$4.9 \times 10^4 \pm 6.6 \times 10^1$
					B	$1.5 \times 10^7 \pm 1.5 \times 10^4$	$8.4 \times 10^6 \pm 1.1 \times 10^4$	$2.5 \times 10^4 \pm 6.2 \times 10^2$
140	<2.0	<0.7	<1.6	<3.2	S	$5.7 \times 10^4 \pm 5.7 \times 10^1$	$5.2 \times 10^4 \pm 5.5 \times 10^1$	$3.2 \times 10^4 \pm 4.3 \times 10^1$
					B	$1.5 \times 10^7 \pm 1.5 \times 10^4$	$8.4 \times 10^6 \pm 1.1 \times 10^4$	$1.8 \times 10^4 \pm 5.2 \times 10^2$
150	<1.9	<0.7	<1.6	<3.2	S	$4.4 \times 10^4 \pm 4.4 \times 10^1$	$4.0 \times 10^4 \pm 4.2 \times 10^1$	$2.3 \times 10^4 \pm 3.2 \times 10^1$
					B	$1.5 \times 10^7 \pm 1.5 \times 10^4$	$8.4 \times 10^6 \pm 1.1 \times 10^4$	$1.5 \times 10^4 \pm 4.7 \times 10^2$
160	<2.0	<0.7	<1.6	<3.2	S	$3.2 \times 10^4 \pm 3.2 \times 10^1$	$1.4 \times 10^4 \pm 3.1 \times 10^1$	$7.2 \times 10^3 \pm 2.4 \times 10^1$
					B	$1.5 \times 10^7 \pm 1.5 \times 10^4$	$8.4 \times 10^6 \pm 1.1 \times 10^4$	$1.0 \times 10^4 \pm 4.8 \times 10^2$
180	<2.0	<0.6	<1.6	<3.2	S	$1.5 \times 10^4 \pm 1.5 \times 10^1$	$4.4 \times 10^3 \pm 1.4 \times 10^1$	$2.7 \times 10^3 \pm 1.0 \times 10^1$
					B	$1.5 \times 10^7 \pm 1.5 \times 10^4$	$8.4 \times 10^6 \pm 1.1 \times 10^4$	$1.5 \times 10^4 \pm 4.0 \times 10^2$
200	<2.0	<0.7	<1.6	<3.2	S	$4.9 \times 10^3 \pm 4.9 \times 10^0$	$6.1 \times 10^2 \pm 4.7 \times 10^0$	$3.7 \times 10^2 \pm 3.7 \times 10^0$
					B	$1.5 \times 10^7 \pm 1.5 \times 10^4$	$8.4 \times 10^6 \pm 1.1 \times 10^4$	$1.8 \times 10^4 \pm 4.7 \times 10^2$
220	<2.0	<0.7	<1.6	<3.2	S	$6.7 \times 10^2 \pm 6.7 \times 10^{-1}$	$8.1 \times 10^1 \pm 6.4 \times 10^{-1}$	$4.9 \times 10^1 \pm 5.0 \times 10^{-1}$
					B	$1.5 \times 10^7 \pm 1.5 \times 10^4$	$8.4 \times 10^6 \pm 1.1 \times 10^4$	$2.2 \times 10^4 \pm 5.2 \times 10^2$

Table 6. Event selections at the ZH threshold, for each mass point. The rightmost columns show the number of events for no applied selection, after the preselection criteria, and after the final selection criteria, for both signal (S) and background (B).

$t\bar{t}$ threshold

m_a [GeV]	M_{cut}	$ \cos\theta_{\gamma_1} $	$ \phi_{\gamma_1} $	$\Delta\alpha_{\gamma_1\gamma_2}$		No selection	Preselection	Final selection
5	<2.0	<1.0	<1.6	<0.1	S	$5.4 \times 10^4 \pm 5.4 \times 10^1$	$5.0 \times 10^4 \pm 5.2 \times 10^1$	$3.5 \times 10^4 \pm 4.4 \times 10^1$
					B	$1.8 \times 10^6 \pm 1.8 \times 10^3$	$1.0 \times 10^6 \pm 1.4 \times 10^3$	$3.2 \times 10^3 \pm 7.6 \times 10^1$
10	<2.0	<1.0	<1.6	<0.2	S	$5.4 \times 10^4 \pm 5.4 \times 10^1$	$4.9 \times 10^4 \pm 5.2 \times 10^1$	$3.5 \times 10^4 \pm 4.4 \times 10^1$
					B	$1.8 \times 10^6 \pm 1.8 \times 10^3$	$1.0 \times 10^6 \pm 1.4 \times 10^3$	$5.2 \times 10^3 \pm 9.6 \times 10^1$
25	<2.0	<1.0	<1.6	<0.4	S	$5.4 \times 10^4 \pm 5.4 \times 10^1$	$4.8 \times 10^4 \pm 5.1 \times 10^1$	$2.9 \times 10^4 \pm 4.0 \times 10^1$
					B	$1.8 \times 10^6 \pm 1.8 \times 10^3$	$1.0 \times 10^6 \pm 1.4 \times 10^3$	$5.7 \times 10^3 \pm 1.0 \times 10^2$
50	<2.0	<1.0	<1.1	<0.8	S	$5.1 \times 10^4 \pm 5.1 \times 10^1$	$4.6 \times 10^4 \pm 4.9 \times 10^1$	$2.3 \times 10^4 \pm 3.4 \times 10^1$
					B	$1.8 \times 10^6 \pm 1.8 \times 10^3$	$1.0 \times 10^6 \pm 1.4 \times 10^3$	$4.5 \times 10^3 \pm 9.0 \times 10^1$
60	<2.0	<1.0	<1.2	<1.0	S	$5.0 \times 10^4 \pm 5.0 \times 10^1$	$4.5 \times 10^4 \pm 4.8 \times 10^1$	$2.6 \times 10^4 \pm 3.6 \times 10^1$
					B	$1.8 \times 10^6 \pm 1.8 \times 10^3$	$1.0 \times 10^6 \pm 1.4 \times 10^3$	$5.3 \times 10^3 \pm 9.7 \times 10^1$
70	<2.0	<1.0	<1.1	<1.1	S	$4.9 \times 10^4 \pm 4.9 \times 10^1$	$4.4 \times 10^4 \pm 4.6 \times 10^1$	$2.2 \times 10^4 \pm 3.3 \times 10^1$
					B	$1.8 \times 10^6 \pm 1.8 \times 10^3$	$1.0 \times 10^6 \pm 1.4 \times 10^3$	$3.9 \times 10^3 \pm 8.4 \times 10^1$
80	<2.0	<1.0	<1.1	<1.3	S	$4.7 \times 10^4 \pm 4.7 \times 10^1$	$4.2 \times 10^4 \pm 4.4 \times 10^1$	$2.3 \times 10^4 \pm 3.3 \times 10^1$
					B	$1.8 \times 10^6 \pm 1.8 \times 10^3$	$1.0 \times 10^6 \pm 1.4 \times 10^3$	$4.0 \times 10^3 \pm 8.5 \times 10^1$
90	<2.0	<1.0	<1.2	<1.3	S	$4.5 \times 10^4 \pm 4.5 \times 10^1$	$4.1 \times 10^4 \pm 4.3 \times 10^1$	$2.1 \times 10^4 \pm 3.1 \times 10^1$
					B	$1.8 \times 10^6 \pm 1.8 \times 10^3$	$1.0 \times 10^6 \pm 1.4 \times 10^3$	$3.6 \times 10^3 \pm 8.1 \times 10^1$
100	<2.0	<1.0	<1.2	<1.5	S	$4.2 \times 10^4 \pm 4.2 \times 10^1$	$3.9 \times 10^4 \pm 4.1 \times 10^1$	$2.1 \times 10^4 \pm 3.0 \times 10^1$
					B	$1.8 \times 10^6 \pm 1.8 \times 10^3$	$1.0 \times 10^6 \pm 1.4 \times 10^3$	$3.9 \times 10^3 \pm 8.4 \times 10^1$
120	<2.0	<1.0	<1.3	<1.8	S	$3.7 \times 10^4 \pm 3.7 \times 10^1$	$3.3 \times 10^4 \pm 3.5 \times 10^1$	$2.1 \times 10^4 \pm 2.8 \times 10^1$
					B	$1.8 \times 10^6 \pm 1.8 \times 10^3$	$1.0 \times 10^6 \pm 1.4 \times 10^3$	$4.2 \times 10^3 \pm 8.7 \times 10^1$
140	<2.0	<1.0	<1.3	<2.0	S	$3.0 \times 10^4 \pm 3.0 \times 10^1$	$2.7 \times 10^4 \pm 2.9 \times 10^1$	$1.7 \times 10^4 \pm 2.3 \times 10^1$
					B	$1.8 \times 10^6 \pm 1.8 \times 10^3$	$1.0 \times 10^6 \pm 1.4 \times 10^3$	$3.9 \times 10^3 \pm 8.4 \times 10^1$
150	<2.0	<1.0	<1.2	<2.0	S	$2.7 \times 10^4 \pm 2.7 \times 10^1$	$2.5 \times 10^4 \pm 2.6 \times 10^1$	$1.4 \times 10^4 \pm 1.9 \times 10^1$
					B	$1.8 \times 10^6 \pm 1.8 \times 10^3$	$1.0 \times 10^6 \pm 1.4 \times 10^3$	$3.0 \times 10^3 \pm 7.3 \times 10^1$
160	<2.0	<1.0	<1.2	<2.1	S	$2.4 \times 10^4 \pm 2.4 \times 10^1$	$2.2 \times 10^4 \pm 2.3 \times 10^1$	$1.3 \times 10^4 \pm 1.8 \times 10^1$
					B	$1.8 \times 10^6 \pm 1.8 \times 10^3$	$1.0 \times 10^6 \pm 1.4 \times 10^3$	$2.9 \times 10^3 \pm 7.2 \times 10^1$
180	<2.0	<0.7	<1.6	<3.2	S	$1.9 \times 10^4 \pm 1.9 \times 10^1$	$1.7 \times 10^4 \pm 1.8 \times 10^1$	$1.1 \times 10^4 \pm 1.4 \times 10^1$
					B	$1.8 \times 10^6 \pm 1.8 \times 10^3$	$1.0 \times 10^6 \pm 1.4 \times 10^3$	$2.8 \times 10^3 \pm 7.1 \times 10^1$
200	<2.0	<0.7	<1.6	<3.2	S	$1.4 \times 10^4 \pm 1.4 \times 10^1$	$1.3 \times 10^4 \pm 1.4 \times 10^1$	$8.0 \times 10^3 \pm 1.1 \times 10^1$
					B	$1.8 \times 10^6 \pm 1.8 \times 10^3$	$1.0 \times 10^6 \pm 1.4 \times 10^3$	$2.1 \times 10^3 \pm 6.1 \times 10^1$
220	<2.0	<0.7	<1.6	<3.2	S	$1.0 \times 10^4 \pm 1.0 \times 10^1$	$9.5 \times 10^3 \pm 1.0 \times 10^1$	$5.8 \times 10^3 \pm 7.8 \times 10^0$
					B	$1.8 \times 10^6 \pm 1.8 \times 10^3$	$1.0 \times 10^6 \pm 1.4 \times 10^3$	$1.8 \times 10^3 \pm 5.7 \times 10^1$
240	<2.0	<0.7	<1.6	<3.2	S	$7.2 \times 10^3 \pm 7.2 \times 10^0$	$6.5 \times 10^3 \pm 6.8 \times 10^0$	$4.0 \times 10^3 \pm 5.4 \times 10^0$
					B	$1.8 \times 10^6 \pm 1.8 \times 10^3$	$1.0 \times 10^6 \pm 1.4 \times 10^3$	$1.6 \times 10^3 \pm 5.3 \times 10^1$
300	<2.0	<0.7	<1.6	<3.2	S	$1.3 \times 10^4 \pm 1.3 \times 10^0$	$1.1 \times 10^3 \pm 1.2 \times 10^0$	$7.0 \times 10^2 \pm 9.4 \times 10^{-1}$
					B	$1.8 \times 10^6 \pm 1.8 \times 10^3$	$1.0 \times 10^6 \pm 1.4 \times 10^3$	$1.5 \times 10^3 \pm 5.1 \times 10^1$
320	<2.0	<0.7	<1.6	<3.2	S	$4.5 \times 10^2 \pm 4.5 \times 10^{-1}$	$4.1 \times 10^2 \pm 4.3 \times 10^{-1}$	$4.9 \times 10^1 \pm 3.3 \times 10^{-1}$
					B	$1.8 \times 10^6 \pm 1.8 \times 10^3$	$1.0 \times 10^6 \pm 1.4 \times 10^3$	$1.5 \times 10^3 \pm 5.1 \times 10^1$

Table 7. Event selections at the $t\bar{t}$ threshold, for each mass point. The rightmost columns show the number of events for no applied selection, after the preselection criteria, and after the final selection criteria, for both signal (S) and background (B).

References

- [1] E.S. Group, *The European Strategy for Particle Physics: 2026 Update - Recommendations by the European Strategy Group (ESG)*, Tech. Rep. <https://cds.cern.ch/record/2950531>, CERN, Geneva, Switzerland (2025).
- [2] FCC collaboration, *FCC-ee: The Lepton Collider: Future Circular Collider Conceptual Design Report Volume 2*, *Eur. Phys. J. ST* **228** (2019) 261.
- [3] FCC collaboration, *Future Circular Collider Feasibility Study Report: Volume 1, Physics, Experiments, Detectors*, *Eur. Phys. J. C* **85** (2025) 1468 [[2505.00272](#)].
- [4] FCC collaboration, *Future Circular Collider Feasibility Study Report: Volume 2, Accelerators, Technical Infrastructure and Safety*, *Eur. Phys. J. ST* **234** (2025) 5713 [[2505.00274](#)].
- [5] A. Blondel et al., *Searches for long-lived particles at the future FCC-ee*, *Front. in Phys.* **10** (2022) 967881 [[2203.05502](#)].
- [6] R.D. Peccei and H.R. Quinn, *CP Conservation in the Presence of Instantons*, *Phys. Rev. Lett.* **38** (1977) 1440.
- [7] R.D. Peccei and H.R. Quinn, *Constraints Imposed by CP Conservation in the Presence of Instantons*, *Phys. Rev. D* **16** (1977) 1791.
- [8] S. Weinberg, *A New Light Boson?*, *Phys. Rev. Lett.* **40** (1978) 223.
- [9] F. Wilczek, *Problem of Strong P and T Invariance in the Presence of Instantons*, *Phys. Rev. Lett.* **40** (1978) 279.
- [10] M. Bauer, M. Neubert and A. Thamm, *Collider Probes of Axion-Like Particles*, *JHEP* **12** (2017) 044 [[1708.00443](#)].
- [11] M. Bauer, M. Heiles, M. Neubert and A. Thamm, *Axion-Like Particles at Future Colliders*, *Eur. Phys. J. C* **79** (2019) 74 [[1808.10323](#)].
- [12] C.B. Adams et al., *Axion Dark Matter*, in *Snowmass 2021*, 3, 2022 [[2203.14923](#)].
- [13] G. Armando, P. Panci, J. Weiss and R. Ziegler, *Leptonic ALP portal to the dark sector*, *Phys. Rev. D* **109** (2024) 055029 [[2310.05827](#)].
- [14] S. Allen, A. Blackburn, O. Cardenas, Z. Messenger, N.H. Nguyen and B. Shuve, *Electroweak axion portal to dark matter*, *Phys. Rev. D* **110** (2024) 095010 [[2405.02403](#)].
- [15] FASER collaboration, *Shining light on the dark sector: search for axion-like particles and other new physics in photonic final states with FASER*, *JHEP* **01** (2025) 199 [[2410.10363](#)].
- [16] BESIII collaboration, *Search for diphoton decays of an axionlike particle in radiative J/ψ decays*, *Phys. Rev. D* **110** (2024) L031101 [[2404.04640](#)].
- [17] BESIII collaboration, *Search for an axion-like particle in radiative J/ψ decays*, *Phys. Lett. B* **838** (2023) 137698 [[2211.12699](#)].
- [18] ATLAS collaboration, *Measurement of light-by-light scattering and search for axion-like particles with 2.2 nb^{-1} of Pb+Pb data with the ATLAS detector*, *JHEP* **03** (2021) 243 [[2008.05355](#)].
- [19] ATLAS collaboration, *Search for boosted diphoton resonances in the 10 to 70 GeV mass range using 138 fb^{-1} of 13 TeV pp collisions with the ATLAS detector*, *JHEP* **07** (2023) 155 [[2211.04172](#)].

- [20] CMS collaboration, *Evidence for light-by-light scattering and searches for axion-like particles in ultraperipheral PbPb collisions at $\sqrt{s_{NN}} = 5.02$ TeV*, *Phys. Lett. B* **797** (2019) 134826 [[1810.04602](#)].
- [21] CMS collaboration, *Search for new resonances decaying to pairs of merged diphotons in proton-proton collisions at $\sqrt{s} = 13$ TeV*, *Phys. Rev. Lett.* **134** (2025) 041801 [[2405.00834](#)].
- [22] TOTEM, CMS collaboration, *Search for high-mass exclusive diphoton production with tagged protons in proton-proton collisions at $\sqrt{s} = 13$ TeV*, *Phys. Rev. D* **110** (2024) 012010 [[2311.02725](#)].
- [23] X. Cid Vidal, A. Mariotti, D. Redigolo, F. Sala and K. Tobioka, *New Axion Searches at Flavor Factories*, *JHEP* **01** (2019) 113 [[1810.09452](#)].
- [24] LHCb collaboration, *Search for resonances decaying to photon pairs with masses between 4.9 and 19.4 GeV*, *Submitted to Phys. Rev. Lett.* (2025) [[2507.14390](#)].
- [25] NA64 collaboration, *Search for Axionlike and Scalar Particles with the NA64 Experiment*, *Phys. Rev. Lett.* **125** (2020) 081801 [[2005.02710](#)].
- [26] J. Blumlein et al., *Limits on neutral light scalar and pseudoscalar particles in a proton beam dump experiment*, *Z. Phys. C* **51** (1991) 341.
- [27] B. Döbrich, J. Jaeckel and T. Spadaro, *Light in the beam dump - ALP production from decay photons in proton beam-dumps*, *JHEP* **05** (2019) 213 [[1904.02091](#)].
- [28] J.D. Bjorken, S. Ecklund, W.R. Nelson, A. Abashian, C. Church, B. Lu et al., *Search for Neutral Metastable Penetrating Particles Produced in the SLAC Beam Dump*, *Phys. Rev. D* **38** (1988) 3375.
- [29] CHARM collaboration, *Search for Axion Like Particle Production in 400-GeV Proton - Copper Interactions*, *Phys. Lett. B* **157** (1985) 458.
- [30] F. Capozzi, B. Dutta, G. Gung, W. Jang, I.M. Shoemaker, A. Thompson et al., *New constraints on ALP couplings to electrons and photons from ArgoNeuT and the MiniBooNE beam dump*, *Phys. Rev. D* **108** (2023) 075019 [[2307.03878](#)].
- [31] A. Caputo, H.-T. Janka, G. Raffelt and E. Vitagliano, *Low-Energy Supernovae Severely Constrain Radiative Particle Decays*, *Phys. Rev. Lett.* **128** (2022) 221103 [[2201.09890](#)].
- [32] J. de Blas et al., *Physics Briefing Book: Input for the 2026 update of the European Strategy for Particle Physics*, vol. 8 of *CERN Yellow Reports: Monographs*, CERN (11, 2025), [10.17181/CERN.35CH.2O2P](#), [[2511.03883](#)].
- [33] G. Polesello, *Sensitivity of the FCC-ee to decay of an axion-like particle into two photons*, *JHEP* **06** (2025) 239 [[2502.08411](#)].
- [34] P. Rebello Teles, D. d'Enterria, V.P. Gonçalves and D.E. Martins, *Searches for axionlike particles via $\gamma\gamma$ fusion at future $e+e-$ colliders*, *Phys. Rev. D* **109** (2024) 055003 [[2310.17270](#)].
- [35] K. Mimasu and V. Sanz, *ALPs at Colliders*, *JHEP* **06** (2015) 173 [[1409.4792](#)].
- [36] J. Alwall, M. Herquet, F. Maltoni, O. Mattelaer and T. Stelzer, *MadGraph 5 : Going Beyond*, *JHEP* **06** (2011) 128 [[1106.0522](#)].
- [37] T. Sjöstrand, S. Ask, J.R. Christiansen, R. Corke, N. Desai, P. Ilten et al., *An introduction to PYTHIA 8.2*, *Comput. Phys. Commun.* **191** (2015) 159 [[1410.3012](#)].

- [38] DELPHES 3 collaboration, *DELPHES 3, A modular framework for fast simulation of a generic collider experiment*, *JHEP* **02** (2014) 057 [[1307.6346](#)].
- [39] IDEA STUDY GROUP collaboration, *The IDEA detector concept for FCC-ee*, [2502.21223](#).
- [40] M. Dam, *Detector requirements, design, and technologies for the FCC-ee Higgs, electroweak, and top factory*, *Nucl. Instrum. Meth. A* **1080** (2025) 170648 [[2505.06781](#)].
- [41] <https://github.com/HEP-FCC/FCC-config/tree/winter2023/FCCEe>.
- [42] C. Helsens, E. Perez, M. Selvaggi, V. Volkl, L. Forthomme and J. Munch Torndal, *Hep-fcc/fccanalyses: v0.11.0*, May, 2025. 10.5281/zenodo.15528870.
- [43] G. Punzi, *Sensitivity of searches for new signals and its optimization*, *eConf* **C030908** (2003) MODT002 [[physics/0308063](#)].
- [44] CMS collaboration, *The CMS Statistical Analysis and Combination Tool: Combine*, *Comput. Softw. Big Sci.* **8** (2024) 19 [[2404.06614](#)].
- [45] W. Verkerke and D.P. Kirkby, *The RooFit toolkit for data modeling*, *eConf* **C0303241** (2003) MOLT007 [[physics/0306116](#)].
- [46] L. Moneta, K. Belasco, K.S. Cranmer, S. Kreiss, A. Lazzaro, D. Piparo et al., *The RooStats Project*, *PoS ACAT2010* (2010) 057 [[1009.1003](#)].
- [47] A.L. Read, *Presentation of search results: The CL_s technique*, *J. Phys. G* **28** (2002) 2693.
- [48] T. Junk, *Confidence level computation for combining searches with small statistics*, *Nucl. Instrum. Meth. A* **434** (1999) 435 [[hep-ex/9902006](#)].
- [49] G. Cowan, K. Cranmer, E. Gross and O. Vitells, *Asymptotic formulae for likelihood-based tests of new physics*, *Eur. Phys. J. C* **71** (2011) 1554 [[1007.1727](#)].
- [50] C. O’Hare, “cajohare/axionlimits: Axionlimits.” <https://cajohare.github.io/AxionLimits/>, July, 2020. 10.5281/zenodo.3932430.
- [51] G. Cacciapaglia, A. Deandrea, A.M. Iyer and K. Sridhar, *Tera-Z stage at future colliders and light composite axionlike particles*, *Phys. Rev. D* **105** (2022) 015020 [[2104.11064](#)].